A&A 473, 279–289 (2007)
DOI: 10.1051/0004-6361:20067011

Astronomy & Astrophysics

Spectrophotometric analysis of Ellerman bombs in the Ca II, Hα, and UV range

E. Pariat[1,2,3], B. Schmieder[1], A. Berlicki[4], Y. Deng[5], N. Mein[1], A. López Ariste[6], and S. Wang[7]

[1] LESIA, Observatoire de Paris - Meudon, 92195 Meudon Cedex, France
e-mail: etienne.pariat@obspm.fr
[2] Université Paris 7 - Denis Diderot, 75251 Paris Cedex 05, France
[3] Naval Research Laboratory, Space Science Division, 20375 Washington, DC, USA
[4] Astronomical Institute, Wrocław University, 51-622 Wrocław, Poland
[5] National Astronomical Observatories, Chinese Academy of Sciences, 100012 Beijing, PR China
[6] THEMIS - CNRS UPS 833, C/ vía Láctea s/n, 38200 La Laguna, Tenerife, Spain
[7] Department of Astronomy, Beijing Normal University, Beijing 100875, PR China

Received 22 December 2006 / Accepted 25 June 2007

ABSTRACT

Context. Even if Ellerman bombs have been observed in the Hα line within emerging magnetic flux regions since the early 20th century, their origin and the mechanisms that lead to their formation have been strongly debated. Recently, new arguments in favor of chromospheric magnetic reconnection have been advanced. Ellerman bombs seem to be the signature of reconnections that take place during the emergence of the magnetic field.

Aims. We have observed an active region presenting emergence of magnetic flux. We detected and studied Ellerman bombs in two chromospheric lines: Ca II 8542 Å and Hα. We investigated the link between Ellerman bombs and other structures and phenomena appearing in an emerging active region: UV bright points, arch filament systems, and magnetic topology.

Methods. On August 3, 2004, we performed multi-wavelength observations of the active region NOAA 10655. This active region was the target of SoHO Joint Observation Program 157. Both SoHO/MDI and TRACE (195 Å and 1600 Å) were used. Simultaneously, we observed in the Ca II and Na D1 lines with the spectro-imager MSDP mode of THEMIS. Alternately to the MSDP, we used the MTR spectropolarimeter on THEMIS to observe in Hα and in the Fe I doublet at 6302 Å. We derived the magnetic field vectors around some Ellerman bombs.

Results. We present the first images of EBs in the Ca II line and confirm that Ellerman bombs can indeed be observed in the Ca II line, presenting the same "moustache" geometry profiles as in the Hα line, but with a narrower central absorption in the Ca II line, in which the peaks of emission are around ±0.35 Å. We noticed that the Ellerman bombs observed in the wings of Ca II line have an elongated shape – the length about 50% greater than the width. We derived mean semi-axis lengths of $1.4'' \times 2.0''$. In the UV time profiles of the Ellerman bombs, we noticed successive enhanced emissions. The distribution of lifetimes of these individual impulses presents a strong mode around 210 s. Study of the magnetic topology shows that 9 out of the 13 EBs are located on the inversion line of the longitudinal field and that some typical examples might be associated with a bald patch topology.

Conclusions. We provide new arguments in favor of the reconnection origin of Ellerman bombs. The different individual impulses observed in UV may be related to a bursty mode of reconnection. We also show that this Ca II 8542 Å chromospheric line is a good indicator of Ellerman bombs and can bring new information about these phenomena.

Key words. Sun: magnetic fields – Sun: photosphere – Sun: chromosphere – line: profiles

1. Introduction

Ellerman bombs (EBs) were observed for the first time by Ellerman (1917). These phenomena are typical of emerging magnetic flux regions. They consist of brief emissions that are spatially well localized and observable in the wings of the Hα hydrogen line. The Hα line profile of EBs is characterized by deep absorption at the line center and strong emission in the wings with maximum at Hα ± 1 Å and fading at 5 Å (Severny 1968). This peculiar appearance of EBs is responsible for another name given to these patterns, "moustaches", as reported by Severny (1958).

Georgoulis et al. (2002) extended the knowledge of the EBs from morphological properties to statistical characteristics. Using the observations provided by the *Flare Genesis Experiment* (FGE) launched in 2000 in Antarctica, they reported on:

- the size of the EBs observed at Hα −0.8 Å: elongated structures ($1.1'' \times 1.8''$);
- their location: mainly on the magnetic inversion line;
- their energy spectra: between 10^{26} and 10^{28} erg with a power-law shape with an index of −2.1.

This suggests that EBs may be considered as micro-flares and may contribute significantly to the heating of the low chromosphere in emerging flux regions. The analysis of the photospheric vector magnetograms of this active region obtained by FGE showed, for the first time that the EBs are associated with small bipoles for particular cases: the magnetic vectors having a concave shape (U-shape) at the location of the EBs (Bernasconi et al. 2002). The measurements of Doppler shifts indicate

downflows in the bipoles, at the locations of the EBs, and weak upflows between the bipoles. This suggests that, during the slow flux tube emergence, the dense material inside the tube is falling down.

Bernasconi et al. (2002) propose a sketch of emerging flux tubes with successive U and Ω parts. This idea had already been mentioned by Mandrini et al. (2002). They extrapolated magnetic field lines above an emerging active region using a linear force-free code (developed by Démoulin et al. 1997) to explain the formation of long filaments in an arch filament system (AFS). The U parts would correspond to bald patch regions (Titov et al. 1993) where the magnetic field lines are tangent to the photosphere.

The high spatial and temporal resolution of the FGE data and the measurements of the magnetic vectors allowed them to make significant progress on these topics. Pariat et al. (2004) revisited the FGE data and applied the linear force-free extrapolation code of Démoulin et al. (1997). The magnetic field was found to be extremely fragmented. Nearly all the studied EBs (~87%) were located either on bald patches or on their associated separatrices. This result is a convincing argument for the hypothesis that EBs are due to magnetic reconnection along bald patch separatrices (as in small flares, e.g. Aulanier et al. 1998).

The extrapolation also shows also that the global geometry of the emerging region presents a hierarchy of small undulated loops overlaid by larger loops. Such large overlaying loops were observed in this active region by the *Transition Region and Coronal Explorer* (TRACE) and Yohkoh (Schmieder et al. 2004). Pariat et al. (2004) could identify several undulated flux tubes ("sea-serpent") under an AFS. They find a characteristic length to the undulation and relate this length to the cut-off length of the Rayleigh-Taylor magnetic instability. They propose that this instability helps the tube to lift itself up. This problem is still difficult to solve in simulations (Magara et al. 2005; Isobe et al. 2005; Archontis et al. 2004, 2005).

In addition, recent observations have shown a statistical correlation between EBs observed in the Hα wings and bright points observed in the continuum at 1600 Å by TRACE (Qiu et al. 2000; Georgoulis et al. 2002). This suggests a common energy release in the low chromosphere and around the temperature minimum. Qiu et al. (2000) find a correlation greater than 50% between EBs in Hα wings and UV brightenings observed with TRACE. With FGE data, Georgoulis et al. (2002) showed a similar spatial correlation.

The EBs are detected in other chromospheric lines (Kitai 1983; Fang et al. 2006). As for the Hα line, the main characteristics of EBs spectra are the broad wings, the strong absorption at the center of the lines, and asymmetric wing emission with higher values in the blue. By using thermal and non-thermal semi-empirical atmospheric models (Fang et al. 2006), recent EBs observations of chromospheric line profiles (Hα and Ca II observed with THEMIS) were interpreted as due to the presence of heating in the low chromosphere. The temperature enhancement was found to be about 600 to 1300 K in thermal models and lower for non thermal models. Fang et al. (2006) suggest that EBs may be similar to sub-microflares and that heating is due to magnetic reconnection. MHD studies lead to a similar conclusion.

The work that we present in this paper is based on new observations obtained in August 2004. Observations of the THEMIS spectropolarimeter were coordinated in the frame of the JOP157 (joint observing program on "Bright Points in Active Regions") and involved several space instruments: the *Solar and Heliospheric Observatory* (SoHO) and TRACE. During the 2004 campaign, THEMIS was observing the Ca II 8542 Å and the Na D1 lines with the Multichannel Subtractive Double Pass (MSDP) spectro-imager. We analyzed the characteristics of the Ca II line profile of the EBs that we identified as bright points in TRACE 1600 Å. TRACE observations provided the characteristic lifetime evolution of UV EBs. THEMIS also provided observations of the magnetic vector field in the Fe I doublet around 6302 Å and spectra in the Hα line with the multi-line MTR (French acronym for "MulTi-Raies") spectropolarimetric mode.

These new coordinated observations allowed us to add new inputs to the three questions related to EBs and introduced previously: can EBs be detected in the Ca II line? What is the relationship between EBs and UV bright points? Can the link between the EBs and the bald patch topology deduced from FGE observations be confirmed by other observations?

The paper is organized as follows. Section 2 presents the active region observed (Sect. 2.1), the instruments (Sect. 2.2), and how the EBs were identified (Sect. 2.3). In Sect. 3, we study the link between the EBs observed in Ca II and the UV bright points, and compute the lifetime of the latest. Section 4 is devoted to the computation of the profile of the EB in the Ca II line (Sect. 4.1) and the Hα line (Sect. 4.2). We then study the links between EBs and the 3D magnetic topology in Sect. 5. Finally, in Sect. 6, we summarize the new information provided by our multi-wavelength observations.

2. Observations

2.1. Active region NOAA 10655

In this analysis we have used the observations of the active region (AR) NOAA 10655. This AR was located at S09 E19 on August 3, 2004 and consisted of a big leading spot with a negative magnetic field and a cluster of subsequent spots of positive magnetic field polarity (see Fig. 1). In the central part of the AR, a group of pores with mixed polarities was observed. These polarities were due to emerging magnetic field. Between August 1st and August 4, 2004, the AR presented an increase in the signed magnetic flux. The observations on August 3rd took place in the middle of this emergence process.

In the eastern part of the active region, between the preexisting positive polarity and the new emerging ones, an AFS (Bruzek 1967; Schmieder et al. 1997; Malherbe et al. 1998) is present and can be observed in the Ca II line center image (see Fig. 2). The AFS can also be observed in the wings of the Ca II line. At $\lambda - 0.35$ Å, the top central parts of the AFS are observed. These sections of the AFS are slowly rising and thus present a blue Doppler shift, which explains why they are observed as in absorption in the blue wing of the Ca II line. In contrast, in the red wing, one observes the footpoints of the AFS. where the plasma is flowing down (e.g. Malherbe et al. 1998), as explained by the "leaky bucket" model (Schmieder et al. 1991). This AFS is the signature of the emergence of magnetic flux tubes through the chromosphere (Bruzek 1967; Schmieder et al. 1991). The EBs are frequently observed beneath AFS (Zachariadis et al. 1987).

In addition, some typical chromospheric features associated with a two-ribbon flare can be observed in the Ca II images. The flare started at 8:20 UT and was classed among the B8 class flares from GOES X-ray flux measurements. This flare was presumably triggered by the emergence of magnetic fields, which led to a reconfiguration of the magnetic field of the AR (Heyvaerts et al. 1977). Since the aim of this paper is to study

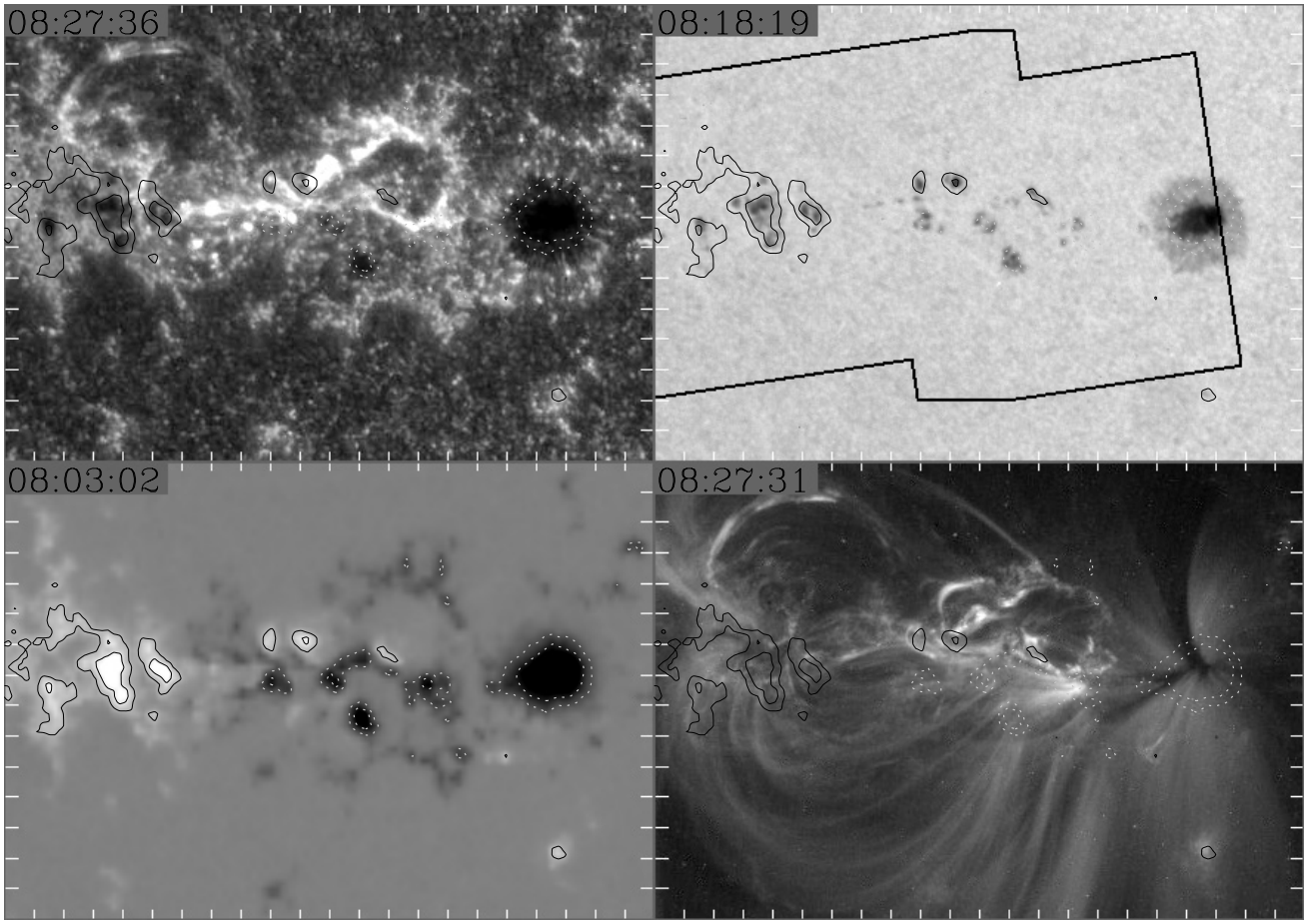

Fig. 1. Images of the active region NOAA 10655 obtained nearly simultaneously on August 3, 2004. TRACE 1600 Å (*top left*) and white-light (*top right*) images. The field of view of the THEMIS/MTR scans is represented in the white light image (thick solid line). SoHO/MDI map of the longitudinal magnetic field (*bottom left*) and TRACE 195 Å image (*bottom right*). The isocontours in each panel are those of the longitudinal magnetic field obtained with SoHO/MDI of ±300, 600 Gauss.

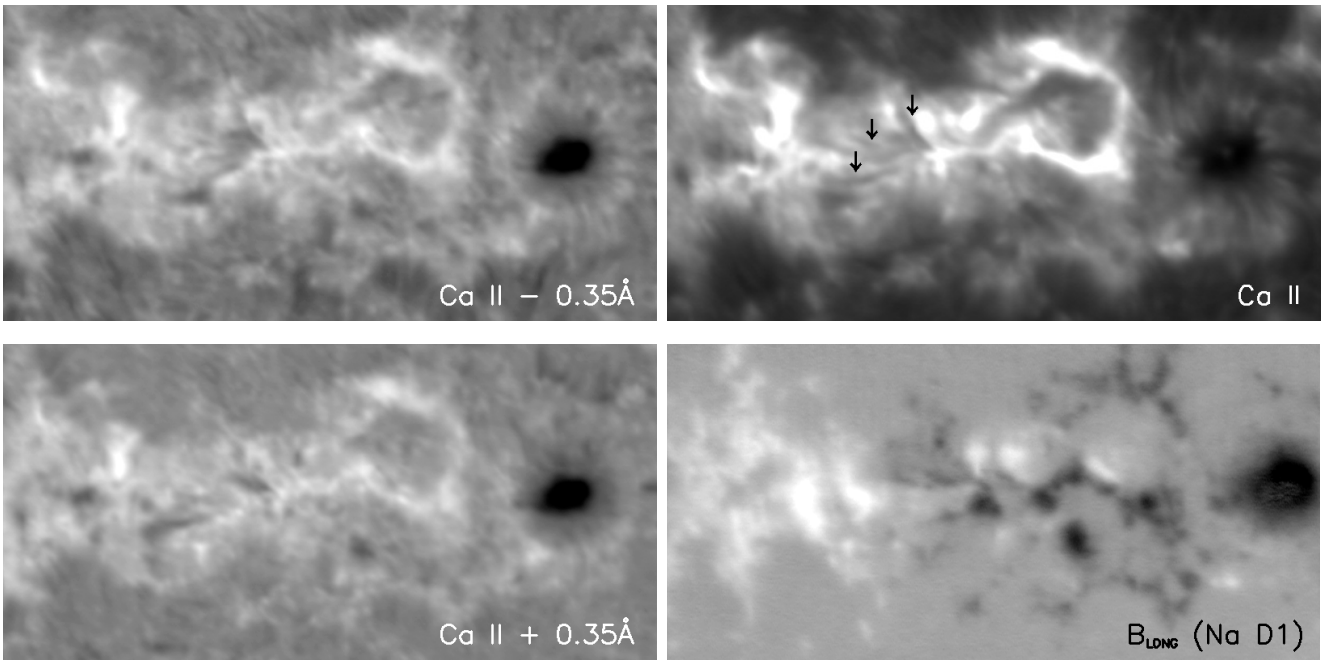

Fig. 2. THEMIS/MSDP observations of the NOAA 10655 on August 3, 2004. The images in Ca II 8542 Å line were obtained at 08:37−08:43 UT, while the map of the longitudinal magnetic field was recorded at 08:22−08:28 UT. The field-of-view of these images is 205″ × 95″. The arrows in the Ca II line center image indicate the position of some arch filaments.

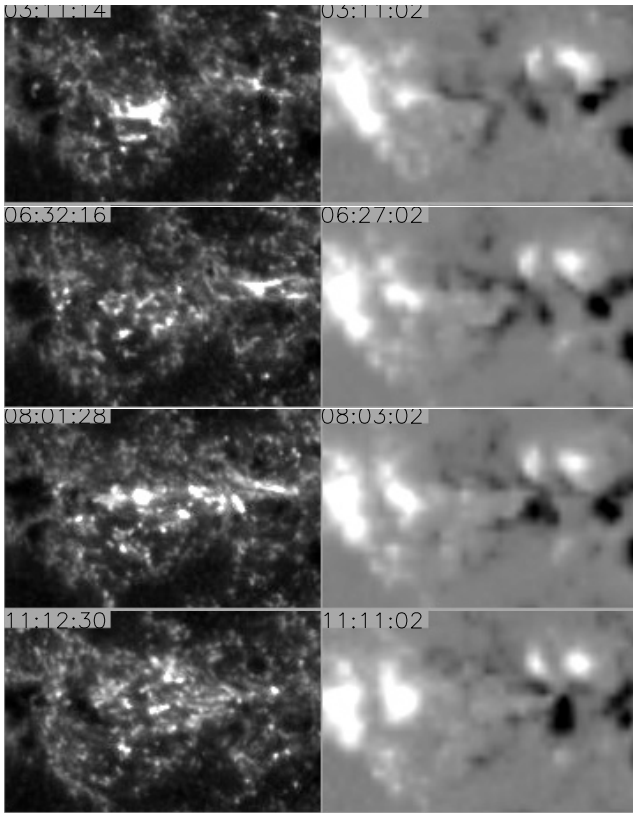

Fig. 3. Evolution of the eastern part of the active region NOAA 10655 observed on August 3, 2004 by TRACE at 1600 Å (*left column*) and the SoHO/MDI magnetograph (*right column*).

of EBs, we did not focus on the emissions due to that particular flare. Thus we did not take features related to that flaring event into consideration.

2.2. Instruments

The observations were done in the framework of the JOP 157 program involving coordinated instruments. For our analysis we used the SoHO/*Michelson Doppler Imager* (MDI; Scherrer et al. 1995) white-light images and magnetograms, along with TRACE (Handy et al. 1999) observations at 195 Å and 1600 Å. TRACE is a high-cadence instrument in different wavelengths and particularly in the continuum at 1600 Å. In this wavelength, the observation cadence was about 35 s and the pixel size was 0.5″. Figure 3 presents the evolution of the AR on August 3rd. The 1600 Å UV image shows the occurrence of numerous bright points. In the meantime, the modification of the distribution of the longitudinal magnetic field is dominated by the coalescence and the increase of opposite-sign magnetic polarities in the center of the active region.

The spectropolarimetric observations of the active region NOAA 10655 were performed with the THEMIS telescope, operating in the MSDP spectro-imager and in the multi-line MTR spectrograph observing modes. THEMIS is a polarization-free, ground-based telescope, designed especially for spectropolarimetric observations.

Detailed descriptions of the specific instrumental set-up of THEMIS in the MSDP observing mode can be found in Mein (2002). The active region was successively observed in the Na I D_1 line, as well as in the chromospheric Ca II 8542 Å line. We obtained the Stokes I and V profiles simultaneously in the 16 MSDP channels. The line-of-sight magnetic flux was derived from $I + V$ and $I - V$ line profiles. We measured Zeeman shifts at each point of the 2D-field of view by a "bisector method" (for details see Berlicki et al. 2006). On August 3rd, 2004 we performed 38 scans of the AR 10655 in Na I D_1 and in Ca II 8542 Å lines. Each scan lasted about 6 min and contains information on the intensity, velocity, and line-of-sight magnetic flux at different wavelengths. Figure 2 presents THEMIS/MSDP observations of AR 10655 obtained around 8:30 UT, in the Ca II 8542 Å and Na I D_1 spectral lines. In the lower right panel we present the line-of-sight magnetic field deduced from I and V Stokes profiles of the Na I D_1 line.

In THEMIS/MTR instrumental mode, it is possible to perform simultaneous observations in several spectral lines. Two particular spectral domains were observed for the present work: the doublet of Fe I around 6302 Å and the Hα line. The spectral binning was 21.6 and 25.8 mÅ per pixel, respectively. Two scans over the active region were performed with this instrument starting at 10:33 UT of this date. The first one was $157'' \times 105''$ in size and centered on the eastern side of the active region, while the second one, starting at 11:37 UT, was $112'' \times 105''$ in size and centered west of the first one. Figure 1 (upper right panel) shows the limits of both scans and their overlapping common region. The spatial pixel size was 0.45″ for a slit width of 1″. The regions were scanned with a constant step of 0.8″.

At each slit-position during the scan, a sequence of 4 images was taken to complete a modulation cycle for the measurement of the full Stokes profiles. The polarimeter positions during that modulation cycle allowed for an accurate retrieval of the Stokes V signal, but they were not enough for Stokes Q and U, which appear polluted with fringes in the data. The reason for this choice of a short modulation cycle was to reduce the scanning time as much as possible, close to one hour per region and too long compared to the average lifetime of EBs (about 10 min).

The simultaneous observation of the chromospheric Hα line and the photospheric Fe I lines allowed the retrieval of magnetic field regions. But the data proved to be quite polluted for a general inversion of the magnetic field vector over all of the scanned regions. For this reason we present only the Stokes V amplitudes (proportional to the longitudinal magnetic flux) and inversions of reduced regions around the EBs for which the number of profiles was small enough to allow for a careful cleaning of fringes. The general data reduction of the data was made with the SQUV package provided by THEMIS (Sainz Dalda & López Ariste 2007). For the inversions we used the PCA inversion code described in López Ariste et al. (2006), also provided to THEMIS observers.

2.3. Identification of Ellerman bombs

All these different data have been coaligned. The coalignement was first done using white-light observations from TRACE and MDI by a fit of the pores and sunspots locations. The parameters modified during the coalignment were the offset of the images, the pixel sizes, and the orientation. We estimate that the error of coalignement is on the order of 2″ (the size of one MDI pixel size). The TRACE white-light images were used to coalign the ground-based THEMIS/MSDP data. The coaligned observations are presented in Fig. 4.

In the emerging flux region, we observed AFS in the Ca II line as absorbing features. As with the usual Hα line, we identified EBs in Ca II by analyzing the profile of this line. The

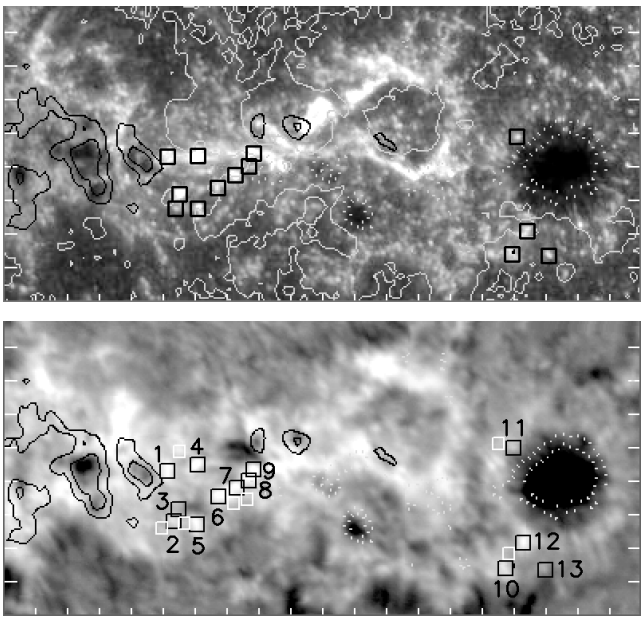

Fig. 4. Central part of NOAA 10655 observed by TRACE at 1600 Å at 8:27 UT (*upper panel*) and THEMIS/MSDP in the Ca II line at −0.35 Å at 8:37 UT (*lower panel*). The isocontours (black line and dotted white line) are those of the longitudinal magnetic field at ±300 and 600 G, determined from SoHO/MDI. Numbered black squares denote the areas where EBs are present. White squares in the bottom panel mark the areas where the nearby Ca II profile has been taken to be subtracted from the profiles of nearest EBs. The continuous gray lines in the upper panel correspond to the inversion line of the longitudinal magnetic field.

EBs were determined as local, brighter areas in the red and blue wings of the Ca II line at ±0.35 Å. We identified 13 locations where an EB is observed as seen in Fig. 4 where they are labeled from "1" to "13". The contrast with the surrounding background intensity is over 0.14 so that we consider that an EB is present. This means that, where an EB is located, the maximum intensity, I, is such that $(I - I_{\rm m})/I_{\rm m} > 0.14$ in one of the wings of the Ca II line, with $I_{\rm m}$ the averaged intensity of the whole image.

We checked that these events were not related to the simultaneous flare. (The events should not be too intense in the line center for example.) These 13 locations do not represent all the EBs present in the active region at that time. We selected these particular events as strong candidates of EBs that can be observed in Ca II.

Using the coaligned TRACE observations, we checked that all of our Ca II EBs were co-spatial with UV bright points. This increased our confidence in the events being observed in Ca II are EBs. Indeed, EBs tend to be well-correlated with UV bright points, where the correlation is even stronger with more intense events (Georgoulis et al. 2002).

In addition, we roughly coaligned the MTR observations obtained at 10:33−11:30 UT and at 11:37−12:22 UT using an image obtained from the continuum in the neighborhood of the Fe I lines and a TRACE white-light image. In the Hα image at ±1 Å, several EBs can be seen as localized emission in one of the wings of the Hα line (see Fig. 5). A large number of EBs are located in the emerging flux area.

From the Ca II line images at ±0.35 Å, we were able to study the morphology and characteristics of the EBs in the Ca II line. For each EB, we estimated its area S, its length l, and its width w. To measure these quantities it was necessary to prescribe a threshold in the emission intensity $I_{\rm t}$. The surface of an EB was determined by all the pixels which intensity I was over $I_{\rm t}$. In the blue wing (resp. red wing), we chose $I_{\rm t}$ equal to 1.18 times (resp. 1.14) the mean intensity. The difference in the threshold values is due to different mean intensities in each wing. More absorption features are present in the blue wing than in the red wing, diminishing the mean intensity in the blue line.

The area S is then equal to the number of pixel multiplied by the pixel surface. The length l is given by the maximum distance between two points located within the EB. The width w is defined as the maximum extension in the direction perpendicular to the length.

It is worth noticing that the estimation of these parameters is extremely sensitive to the choice of $I_{\rm t}$. Nevertheless, following Georgoulis et al. (2002), we estimated the ratio l/w, which is far less dependent on the choice of $I_{\rm t}$. Furthermore, all EBs cannot be seen in both wings of the Ca II line (such as EBs "3" and "11" in the blue wing image). This is why we determined the EB size using only the image where the EB was best observed, i.e. where the contrast was the greatest. We checked that, for most EBs, the results were not too different from one wing to the other, given the used threshold.

As in the Hα line, the EBs observed in Ca II present an elongated shape. On average, the length, l, is 1.49 times greater than their width w. In the Hα line, Nindos & Zirin (1998) report a value ranging from 1.37 to 1.45, and Georgoulis et al. (2002) a ratio of 1.67. With the thresholds given above, we found that the mean length is about 4.1″ and the mean width is 2.8″. Following Georgoulis et al. (2002), if one assumes that EB have an elliptical shape, then its surface S is given by $S = \pi ab$, with a and b the semi-axis lengths. Assuming that $a = 1.49b$, we found that, in average, the typical size of our Ca II EBs is 1.4″ × 2.0″. This is slightly larger than the value of 1.1″ × 1.8″ determined by Georgoulis et al. (2002).

This difference may be due to a bias in the way we selected the Ca II EB since we only took the most apparent events into consideration. On another hand, this difference may also be due to the intrinsic differences in the emission process of each line. Both Ca II and Hα are formed in NLTE conditions, and their sensitivity to thermodynamical parameters of the atmosphere are different. The Ca II line is collisionally controlled and sensitive to the local temperature, whereas Hα is radiatively controlled and sensitive to the local density. When an EB occurs, this difference might lead to different properties in each line emissions.

3. TRACE observations and time evolution of Ellerman bombs

We used the data of TRACE UV continuum at 1600 Å, from 8:00−9:00 UT on August 3, 2004 to study the time evolution of the EBs. In this wavelength, the observation cadence was about 35 s and the pixel size 0.5″. In active region NOAA 10655, 17 positions (the 13 previous points and 4 additional points) were analyzed. Most of these points present simultaneous brightenings in UV and in the wings of the Ca II line. The flux is integrated over a fixed area. Because of the various sizes of EBs, different sizes of boxes were used to count the total intensity of each events, ranging from 15 pixels to 109 pixels. The size of the boxes was taken large enough to prevent errors that may have appeared if the bright point was moving during the period of study. We checked nevertheless that taking a larger or a smaller area (twice the number of pixels) did not change the results significantly.

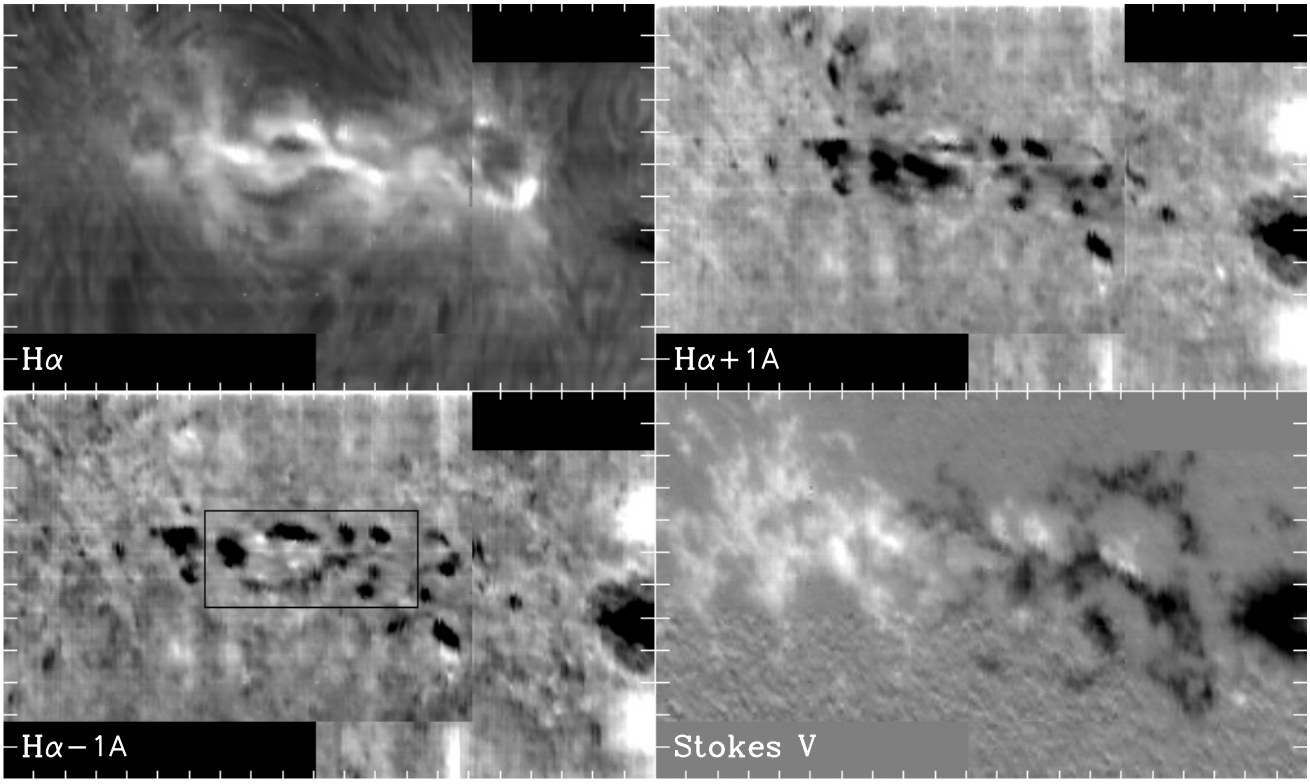

Fig. 5. THEMIS/MTR observations of the NOAA 10655 on August 3, 2004 between 10:33 UT and 12:22 UT. The field-of-view of these images is $218'' \times 122''$: Hα center line (*top left panel*), at +1 Å (*top right panel*), and at −1 Å (*bottom left panel*). The field-of-view of all the images is perfectly co-spatial due to the ability of MTR to observe several lines simultaneously. Stokes V map determined from Fe I line (*bottom right panel*). The black rectangle in the bottom left panel indicates the emerging flux region where several AFs are visible (in the Hα line center image, *top left panel*) and where several EBs occur (see bright points at Hα −1Å, *bottom left panel*).

Studying the time profile of EBs, observed at 1600 Å by TRACE, Qiu et al. (2000) report on the total life time of EBs and on the rising and decaying time of the emission. Using 1−2 s cadence data, they find that the rising time of the EB emission was about 64 s and that the mean decaying time was about 73 s. They also note that fine structures could be detected in the light profile when EBs occurs, the time scale of these profiles ranging from 1 to 5 min. We presently extend this previous study by estimating the statistical properties of these fines structures impulses.

Figure 6 presents two typical normalized time profiles of 1600 Å events. The normalized time profile, $I_{\rm N}$, corresponds to the brightness of the studied event relative to its minimum intensity, $\min_{\rm t}(I)$ during the studied period, with $I(t)$ the integrated flux of the event over the studied region. Thus, $I_{\rm N}$ is equal to: $I_{\rm N}(t) = (I(t) - \min_{\rm t}(I))/\min_{\rm t}(I)$. This allows the variations of contrast with time to be emphasized.

As noted by Qiu et al. (2000), the EB time profiles of the integrated intensity present fine structures. In our data, we have determined the lifetime of the individual impulses present within the time profiles of the 17 UV bright points. From one to five impulses can be observed for each UV bright point. Such individual impulses do not necessarily mean a succession of single EBs.

For example, the upper panel of Fig. 6 presents EB "3", which appeared around 8:08 UT and disappeared around 8:33 UT. This EB presented 2 main impulsive phases peaking at 8:11 UT and 8:27 UT. The lower panel of Fig. 6 shows a long-lived EB (EB "6"), in which five individual impulses can be seen at 8:27, 8:31, 8:35, 8:41, and 8:51 UT.

We found 52 individual impulses within the time evolution of the 17 studied UV bright points. The lifetime of a given bright point corresponds to the time during which the normalized integrated UV flux is above a given threshold. The values for the threshold are adapted to each impulse, depending on the maximum intensity and the eventual occurrence of other impulsions. The distribution of lifetimes for these individual impulses is presented in Fig. 7. If 88% of the impulses have a lifetime between 100 and 430 s, the distribution peaks for lifetimes ranging between 180 and 240 s (3 to 4 min). This strong peak at 210 s indicates that these impulses seem to have a strong preferential lifetime around 3 min 30 s.

4. Chromospheric profiles of the Ellerman bombs

4.1. Observed Ca II 8542 Å line profiles

From the THEMIS/MSDP observations, we reconstructed the profiles of the chromospheric line of Ca II 8542 Å in the instrument-limited wavelength range [−0.5, +0.5] Å. We focused on the areas corresponding to the EBs. The black squares in Fig. 4 are the centers of those areas. For each pixel of the spectral images, the Ca II line profiles were extracted automatically during the processing of THEMIS/MSDP data. We obtained the mean profile for each analyzed area by averaging the profiles coming from the nine pixels contained inside a square box of $0.75'' \times 0.75''$, the pixel size being equal to $0.25''$.

Altogether, we used 13 Ca II 8542 Å line profiles obtained from the observations at 08:37−08:43 UT. In Fig. 8 we present Ca II profiles of chosen EBs and the reference profiles (upper panels). In the bottom panels, we plot these profiles as the result of the difference between the EB Ca II line profile and the nearby

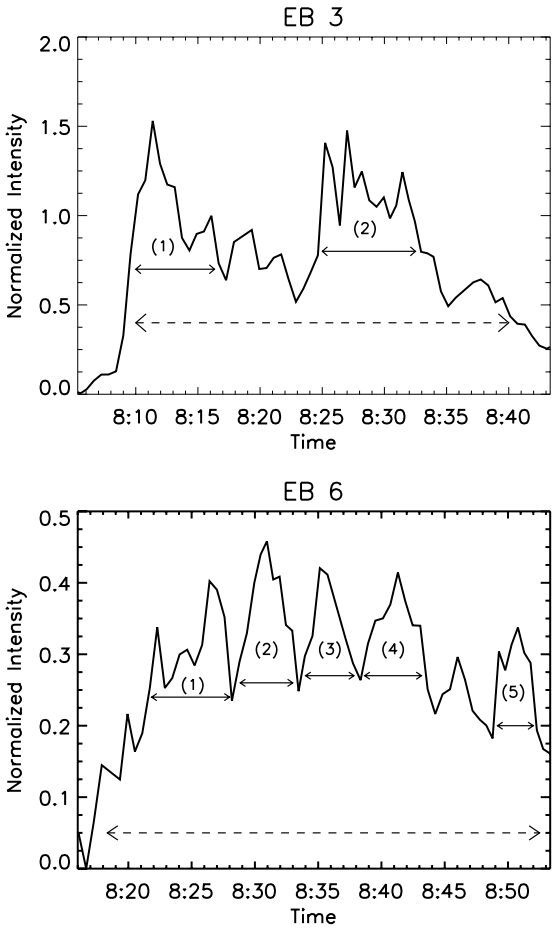

Fig. 6. Two examples of the time evolution of the brightness of EBs observed at 1600 Å (TRACE). These plots are for EB "3" (*upper panel*) and "6" (*lower panel*) (see Fig. 4). The axis of ordinates shows the normalized intensity: the absolute intensity divided by the minimum value minus one. The duration of the EB is indicated by dashed arrows. The EB time profiles present individual impulses (2 for EB "3" and 5 for EB "6"), whose lifetimes are indicated by continuous arrows.

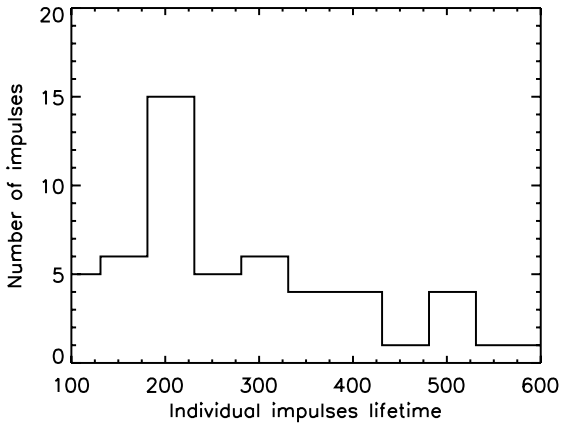

Fig. 7. Histogram of the lifetime of the individual impulses in the EB time profiles observed by TRACE at 1600 Å for the active region NOAA 10655 between 08:11 UT and 08:51 UT. The axis of ordinates corresponds to the number of impulses which lifetime (in second) is given in the axis of abscissas, binned by a factor of 50 s.

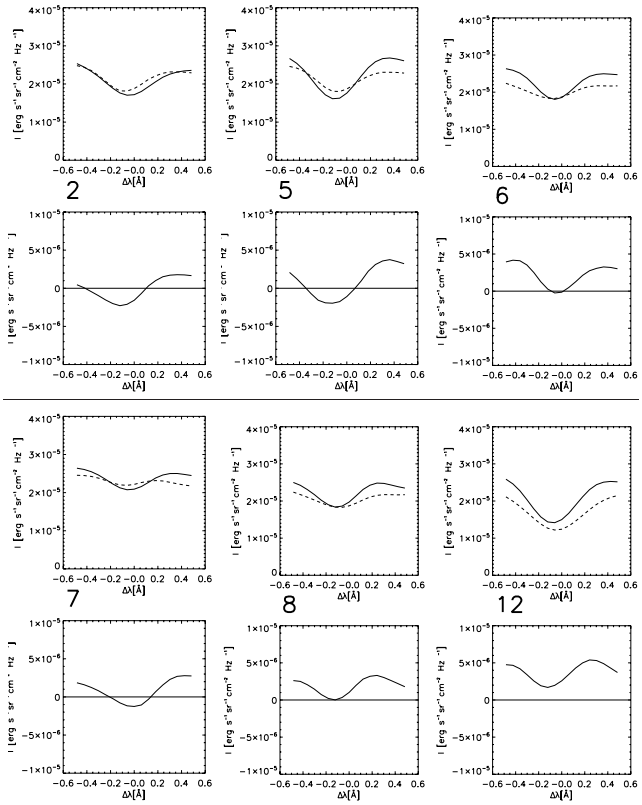

Fig. 8. Ca II 8542 Å profiles of EBs in areas "2", "5", "6", "7", "8", and "12" observed at 08:36–08:43 UT. For each EB – *Upper panels*: bold line: EB profile; dashed line: reference nearby Ca II line profile. *Bottom panels*: EB profiles in the Ca II line, with the nearby profile subtracted.

Ca II profile coming from the chromosphere outside the EBs. These difference profiles are necessary in order to see the excess emission in the wings of the EBs profiles. Since the background profile of emerging flux region tends to be very different from the quiet Sun (e.g. due to global heating by EBs), it is necessary to subtract the profile of a neighboring point (located a few seconds of arc away from the EB). In addition, features like AFs, which are sometimes located above the place where EBs occur, have strong absorption and may mask the real EB profiles. By taking the difference of the EB profile with a neighboring point, the local enhancement of the flux in the wings of the EB profiles becomes more obvious (see Fig. 4). The excess emission was previously reported by Fang et al. (2006) for individual profiles, who observed the enhanced emission in the wings of both Hα and Ca II 8542 Å lines. As in their study, we did not observe a net trend to stronger intensity in the blue wing peak compared to the red wing.

4.2. Observed Hα line profiles

The THEMIS telescope working in the MTR instrumental mode allowed us to perform simultaneous observations in several spectral lines. On August 3, 2004 we studied the Fe I doublet (around 6302 Å) and the hydrogen Hα line. The Hα line profiles were reconstructed with a spectral resolution of 25.8 mÅ within a spectral range ±2.5 Å from the line center. Even if the MTR scans were obtained at 10:33−11:30 UT and at 11:37−12:22 UT, the points observed being located in the emerging flux region, we estimate that the observations of these particular events actually took place between 11:10−11:45 UT.

The intensity calibration of the Hα line profiles were performed using the observed profile of the quiet-Sun area and

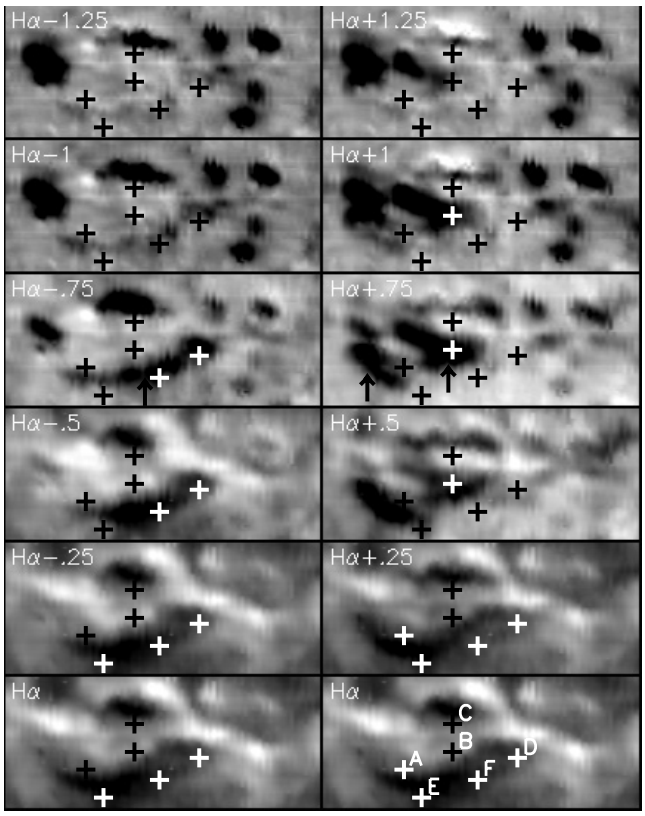

Fig. 9. THEMIS/MTR observations of the NOAA 10655 on August 3, 2004 between 10:33 UT and 11:30 UT (first scan) on the Hα line. Several EBs have been located by a plus sign and labeled from "A" to "F". The field-of-view of these images is $72'' \times 31''$ and corresponds to the area enclose in the black rectangle of Fig. 5. *Left panels*: blue wing of Hα. The dark structures (like the one indicated with an arrow in the Hα −0.75 Å image) correspond to the top of rising archfFilaments. *Right panels*: red wing of Hα. We note downflows within the arch filaments legs (for example those indicated by arrows in the Hα +0.75 Å image).

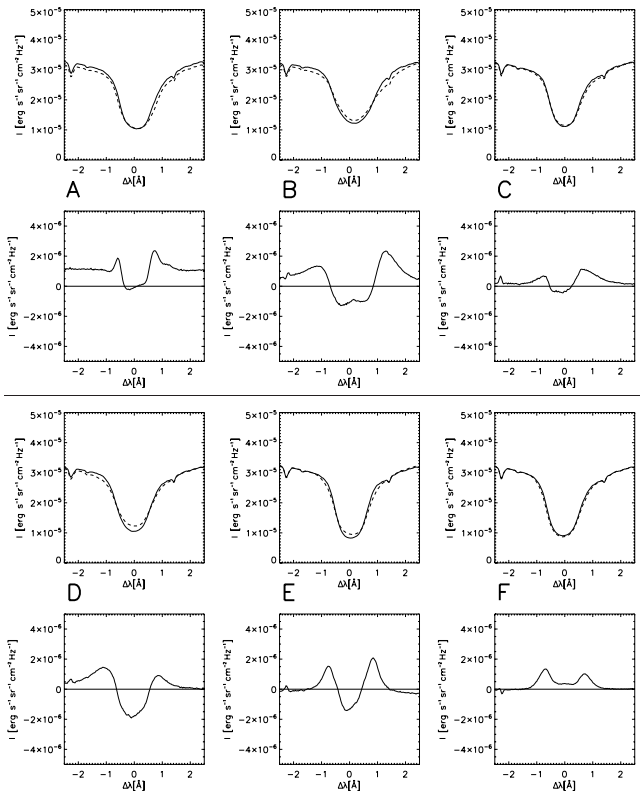

Fig. 10. THEMIS/MTR Hα profiles of the 6 EBs identified in Fig. 9. For each EB – *Upper panels*: bold line: EB profile; dashed line: nearby reference Hα profile. *Bottom panels*: EB profiles in the Hα line, with the nearby profile subtracted.

the reference profile of quiet-Sun obtained by David (1961). In Fig. 9, we present several EBs where we performed a detailed analysis of the Hα line profile. In this figure, an AFS can be observed. As discussed in Sect. 2, following the "leaky bucket" model (Schmieder et al. 1991), the rising tops of the Arch Filaments appear as dark features in the blue wing of the Hα line, whereas the footpoints of the arch filaments are observed in the red wing (the plasma flowing down). The EBs are located beneath these arch filaments.

Here again, it is necessary to subtract the profile of a neighboring point to see the spectral features associated with EBs. Figure 10 (upper panels) presents the Hα line profiles of chosen EBs and the line profiles of the neighboring points. The neighboring points are located very close to the EBs ($\sim$1−2″). In the lower panels of Fig. 10, we present the profiles that result from subtracting the neighboring profile from the EB profile. The most important features of these difference profiles are two peaks located between ±0.7 and ±1.0 Å.

As Hα is an intrinsically narrower line than Ca II, it is natural that the emission excess observed in the wing of the Hα line (around ±1.0 Å) occurs farther from the line center than with the Ca II line (in which the EB emission excess is maximum around ±0.35 Å). For the MSDP spectrograph, which has a relatively narrow bandpass width, the Ca II line is better adapted to observe EBs than the Hα line, whereas Hα is a suitable line in the MTR mode.

5. Magnetic field topology

5.1. Link with the magnetic inversion line

Using the MDI magnetogram coaligned with the THEMIS/MSDP observations, we were able to study the relationship between the location of our 13 Ca II profiles and the magnetic field distribution. In the upper panel of Fig. 4, one can see that, within the limited spatial resolution of the observations, 9 out of 13 EBs ("2", "3", "4", "5", "6", "7", "8", "9", and "12") are located along an inversion line of the photospheric longitudinal field. The remaining ones are generally located close to sunspots. This is in good agreement with previous studies.

Rust & Keil (1992) and Dara et al. (1997) indicate that EBs can generally be found close to an inversion line of the longitudinal magnetic field. Georgoulis et al. (2002) and some previous studies nevertheless have noted that a significant number of EBs cannot be related with any photospheric neutral line. Using the same data set, but considering the vertical component of the magnetic field (normal to the local solar surface), thanks to the vector magnetic field observations of FGE, Pariat et al. (2004) showed that the correlation increased significantly.

Pariat et al. (2004) have also shown that a significant number of EBs that could not be located above inversion lines could be related to the footpoints of separatrices field lines, i.e. in a unipolar region. Here also, 31% of the EBs ("1", "10", "11", and "13") are located in unipolar region close to penumbra of

the main spots. These EBs may be related to separatrices, even if it is impossible to confirm or disprove this in the present study.

Another point of interest is the relation between the EBs observed in MSDP mode at 8:27 UT and the ones observed with MTR around 11:10 UT. It has been previously noted by Zachariadis et al. (1987) that successive EBs tend to occur at the same location. Rather than the same location, the key factor is the same topological environment. Bernasconi et al. (2002) and Nindos & Zirin (1998) have already presented EBs that could be related with moving magnetic features. They show that successive EBs appear at locations that follow the moving magnetic polarity motions.

More generally, EBs tend to follow the magnetic field distribution. As shown in Fig. 11, several EBs observed in Hα can be linked in terms of field distribution to EBs observed in Ca II two hours before. Between these two times, the magnetic field has evolved slightly. But on active region evolution time scales, this two-hour difference is not enough to significantly change the overall magnetic field patterns. Numerous features can be found at both times. For example, the large ">" shape of the inversion line, close to the EBs of Figs. 4 and 11, stayed largely the same between 8:27 UT and 11:11 UT. Within this emerging region and in both observations, a small negative magnetic polarity can also be found within the positive magnetic area.

In Fig. 4, we find that this parasitic polarity was associated with two EBs, labeled "2" and "3". In MTR observations, one sees that this polarity is also located extremely close from two bombs, "A" and "E". Similarly, the EBs "D" and "F", which are located above an inversion line presenting an undulated shape, can be related to the EB numbers "6" and "7". They are located in roughly the same section of the inversion line, around the same undulation. The EB "C" can also be related to EB "4". They are both located close to an inversion line that presents similarities of shape in both observations. Among the EBs that we studied in Hα, only EB "B", located in the middle of the emerging flux region, could not be related to any EB observed in Ca II.

These results are new elements in favor of the hypothesis that the magnetic field distribution and topology are key elements for understanding EBs. The evolution of the magnetic field tends to be rather slow compared to other phenomena appearing in an emerging active region (such as AFSs, EBs, etc.). In addition, the magnetic topology (the field line connectivity) is generally well-conserved even when important photospheric motions are present (e.g. see review by Longcope 2005). Topological structures, like bald patches, may easily explain the recurrence of flaring events such as EBs during several hours.

5.2. Link with bald patches

Pariat et al. (2004) have shown that EBs are more particularly associated with bald patches; topological features where the vertical field is null and where the field lines have a positive curvature – i.e. photospheric U-loops. Not only EBs can be found at bald patch locations but also at the position of the footpoints of the separatrix, the particular field line that goes through a bald patch. This explains why numerous EBs are expected to be located, not only along the inversion line, but also in unipolar regions.

However, the hypothesis that EBs are due to given topological structures (e.g. a bald patch) since these topological features slowly evolve with the magnetic field, explains simply why successive EBs seem to follow the location of the bald patch. To confirm that, we looked at the vector field line topology. Even if

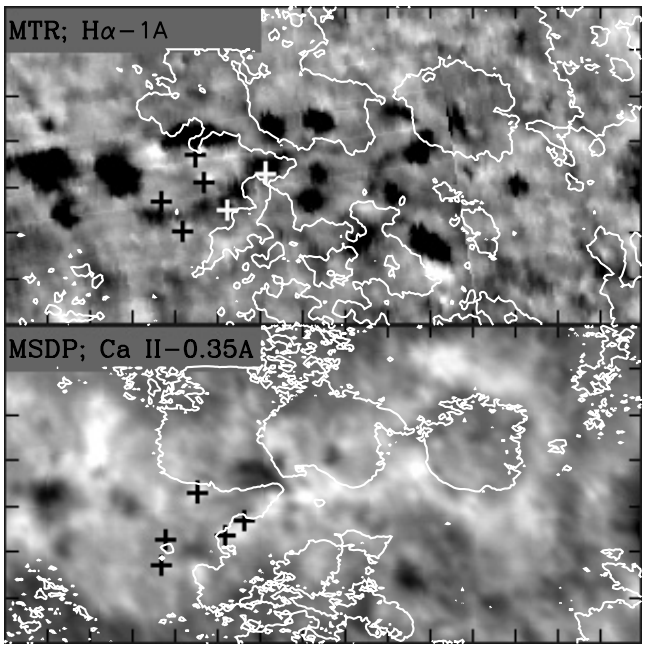

Fig. 11. *Top panel*: THEMIS/MTR Hα observations at -1 Å from the first scan (10:33–11:30 UT). The isocontours correspond to the null value of the Stokes V parameter (from Fe I 6302 Å line) and thus to the neutral line of the longitudinal magnetic field. The 6 crosses locate the position of some EBs presented in Fig. 9. *Bottom panel*: THEMIS/MSDP Ca II -0.35 Å observation at 8:27 UT. The isocontours correspond to the inversion lines of the longitudinal field derived from Na D1. The 5 crosses correspond to the position of the 5 EBs that can be related to those observed in Hα with MTR mode, about 2 h later.

an inversion could not be done for the whole active region, we could perform it for small areas, such as those where EBs occur. In the case of EB "D", we inverted the full Stokes parameters using a PCA-based inversion code (López Ariste et al. 2006).

The inversion procedure results in a full Milne-Eddington model of the atmosphere at each point, including the magnetic field vector and a filling factor that takes into unresolved structures account in the resolution element. In Fig. 12 (top right panel) we present the elevation angle of the magnetic field (angle of the magnetic field vector relative to the plane perpendicular to the line-of-sight; upper right panel) and the longitudinal flux density (bottom right panel, background image) for the region, as well as the azimuth of the field vector in the form of overdrawn segments. The EB "D" occurs along an inversion line of the longitudinal field, since the elevation is null at the location of the EB (the zenith angle is thus equal to $\pi/2$). In addition, Fig. 12 (right panels) shows that the inferred azimuth results in magnetic field vectors that link the opposite magnetic polarities and that are almost perpendicular to the inversion line on the scale of the whole figures. The detailed shape of the inversion line is here governed by the pixel discretization and depends on the pixel's shape and resolution. Even if the present resolution cannot rule out the presence of some weak shear, the vectors are rougthly parallel to the direction of the axis linking the negative magnetic polarity in the bottom left to the positive polarity in the top right part of the figure. Note that two pixels near the center presented both a flux and an azimuth uncorrelated to the one of their neighbors (so their transverse field is not plotted in Fig. 12).

Fit errors after the inversion were on average comprised between $1-2 \times 10^{-3}$ times the intensity of the continuum for the four Stokes parameters, a figure comparable to the original noise

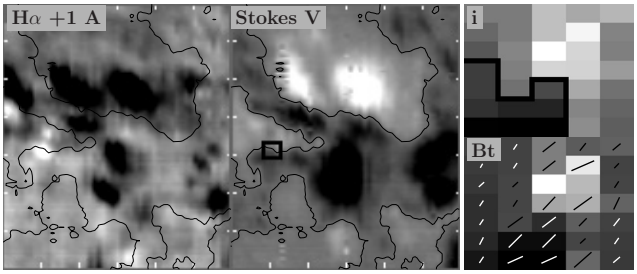

Fig. 12. *Left*: Hα image at ± 1 Å from the second MTR scan (11:37−12:22 UT) of the emerging flux area. *Middle*: location (black box) of the EB "D" (see Fig. 9) on the Stokes *V* map. The field-of-view of these images is $40'' \times 47''$. The isocontours correspond to the null value of the Stokes *V* parameter. Note that around the EB, the inversion line presents some undulations, in the form of "∼", in the vicinity of the black box, respective to the horizontal (left-right) direction. *Right down*: longitudinal magnetogram around the EB. The field-of-view of this image is $4'' \times 3.15''$ and corresponds to the area within the black box in the middle panel. The segment gives the direction of the transverse field. The ambiguity has not been resolved. The length is proportional to the transverse field intensity. *Right up*: elevation angle *i* of the magnetic field (angle of the field relatively to the plane perpendicular to the line-of-sight), coded in levels of gray. White and light grays indicate positive values and thus the magnetic field pointing upward, and black and dark grays refer to negative values and correspond to the magnetic field pointing downward. The bold black line indicates the position of the inversion line. Note that its detailed shape strongly depends on the pixel size and resolution and cannot be directly interpreted.

in the observations. An exception occurs for the two abovementioned pixels for which the fits to Stokes *I* and *V* were well within the average, but the fits to Stokes *Q* and, in particular to Stokes *U*, were completely off with errors beyond 3×10^{-3}. In addition, the profile shape appeared clearly wrong after visual inspection. Most probably, the finite-sized database used for the inversion did not contains an appropriate model for simultaneously fiting the Stokes *V* signature and the *Q* and *U* ones. Priority has been given to Stokes *V* because of its signal amplitude, so a model has been chosen that fits *V* appropriately but not *Q* and *U*. Such an inversion failure affected mostly the azimuth of the two aforementioned pixels, but neither the inclination (which depends on the amplitude of linear polarization but not on its shape) nor the field strength.

For the others pixels, the errors in the inversion were comparable to the noise in the observation, and they translated into error bars for the magnetic parameters. The concentration of the inversion in this small area allowed careful control of error spreading and the error bars in field strength, inclination, and azimuth were comparable to those given in López Ariste et al. (2006). Of particular interest here is the error in azimuth, which in all cases is below 40°, thus confirming that the two polarities both sides of the inversion line are magnetically linked and that, in consequence, the EB occurring here is very likely due to that unveiled flux tube.

Unfortunately, the 180° ambiguity of the transverse field could not be resolved over such a small area. This means that it was not fundamentally possible to discriminate whether the flux tube has a U or an Ω shape. Nevertheless one can note that the magnetic bipole orientation of the flux tube is opposite to the main bipole direction of the active region: the positive polarity for this flux tube is on the west and the negative one at the east, whereas the positive polarity of the active region is located to the east of the negative polarity. In addition, one sees (in Fig. 12, left panel, in the vicinity of the black box) that the inversion line presents a "∼" shape, around the EB. These elements tend to make us believe that U loops are present. Indeed, when the field is potential-like or close to potential, a small magnetic bipole whose orientation is opposite to a main bipole creates a null point and thus U shape loops above the null point (see Sect. 5.1 of Longcope 2005).

When the field is close to potentiality, such magnetic configurations tend to create bald patches; see the classical 3D sketches of bald patches in Titov et al. (1993), Bungey et al. (1996), and the observed bald patch in Aulanier et al. (1998). Thus, even if we cannot completely dismiss the hypothesis that an Ω loop could present here, there are strong reasons to think that the EB observed in Hα is due to and linked with a separatrix and presumably a U loop. The present analysis cannot confirm this result by Pariat et al. (2004), but it nevertheless shows hints of this topology.

6. Conclusion and discussion

We reported on emerging magnetic flux (EMF) in the central part of the active region NOAA 10655. This region was the target of the JOP157 (Joint Observing program on "Bright Points in Active Regions") between August 1 and 4, 2004. New flux started to emerge on August 1st. We analyzed the evolution of the magnetic flux emergence on August 3rd between 03:00 UT and 13:00 UT using MDI, TRACE 1600 Å, and the THEMIS spectropolarimeter. The signatures of this EMF were principally the apparition of mixed polarity magnetic elements with fast velocities leading to the growing of the EMF region. Over the EMF region, a typical AFS was observed.

THEMIS was observing in two modes successively during this time interval. This allowed us to follow the magnetic evolution of the region, and the two modes brought us complementary information on the process of emergence. The MSDP spectrograph observed spectra of two lines: Na D1 and Ca II 8542 Å. With the MTR instrumental mode, we simultaneously observed several absorption lines, in particular the Fe I doublet (6301 Å and 6302 Å) and the Hα line.We were able to derive the Stokes parameters from the Fe I doublet

In the EMF region, we observed several points presenting bright emission in both wings and excess of absorption in the core of Hα and Ca II lines. The peaks of emission are around ± 1 Å in Hα and ± 0.35 Å in Ca II. This is the typical signature of Ellerman bombs (EBs). As in Hα, the EBs observed in Ca II are elongated structures with an average length 1.49 times larger than their width. Assuming an elliptical shape we find that Ca II EB have semi-axis lengths of $1.4'' \times 2.0''$, slightly larger than the values given in previous Hα studies.

The enhanced emission observed in the wings of the chromospheric lines may occur due to heating processes in the EB atmosphere (Severny 1968; Fang et al. 2006). This heating is expected to occur mostly in the lower chromosphere or upper photosphere. Since Hα and Ca II lines are broad lines, formed over a wide range of altitudes in NLTE conditions, more detailed studies of the stratification of the EBs should be needed to couple the profile calculations of both lines and these codes are not yet available. Moreover, in the data of this paper, the two lines are not observed simultaneously in the same EBs.

A very good correspondence has been found between EBs observed in chromospheric lines and in TRACE 1600 Å. Due to the high cadence of TRACE (35 s) we studied the time profiles of 17 EBs. The time profiles show fine structures corresponding

to enhanced emission. The distribution of the computed lifetime of these individual impulses presents a mode at 3 min 30 s.

Following the idea that EBs are due to magnetic reconnection, these reoccurring impulses may be understood as the different phases of a bursty mode of reconnection. A similar hypothesis has been made by Chae et al. (1998) and Ning et al. (2004). Studying other UV wavelengths, such as the Si IV 1393 Å line, they also observed reoccurring bright points with the same typical lifetime. These transition-region explosive events have lifetimes ranging from 1 to 4 min and reoccur at the same location (Ning et al. 2004). This bursty mode of reconnection can be explained in numerical simulation whether by sporadic ejection of plasmoids in the current sheet (e.g. Karpen et al. 1995; Fan et al. 2003) or stimulated by *p*-mode oscillations (Chen & Priest 2006). Indeed, Ning et al. (2004) noted that the recurrence rate of the impulses, ranging from 3 to 5 min, was similar to the period of chromospheric oscillations.

Finally, we studied the magnetic topology of the EBs. They are mostly located along inversion magnetic lines, and they follow the displacement of these lines during the expansion of the EMF. The THEMIS/MTR observations allow us to compute the azimuth of the magnetic field vectors under EBs. We found that the magnetic field vectors are joining the opposite magnetic polarities. In addition, the orientation of the magnetic field bipole suggests that the EBs may be located in a region where the field lines present a U shape.

This particular magnetic topology, named bald patch, is a preferential site for the triggering of magnetic reconnection and thus explains the occurrence of EBs at these types of location simply. It tends to confirm that the emergence of the flux tube does not consist of a large Ω loop but of a succession of U and Ω sections like a "sea serpent", as proposed in Pariat et al. (2004).

In this previous study of the 3D magnetic topology of an emerging region, it was demonstrated how a flux tube could emerge from the sub photosphere in different phases. After the emergence of small sections (2 Mm) of the undulated flux tube, due to the Parker instability, successive reconnections, occurring around the U parts, allow the flux tube to extract itself from the photosphere. The emergence of the tube is then observed through the apparition of AFS. This resistive emergence scenario has recently been corroborated by a 2D MHD numerical simulation (Isobe et al. 2007). EBs appear as the signatures of the magnetic reconnections occurring during the process of emergence.

Acknowledgements. The authors first wish to thank the anonymous referee for very helpful comments. This work was supported by the European Commission through the RTN program (European Solar Magnetism Network,contract HPRN-CT-2002-00313). Part of the work of E.P. was also supported by grants from NASA and NSF. The work of A.B. was supported by the Polish Ministry of Science and Higher Education, grant No. N203 016 32/2287. We also would like to thank the THEMIS team who operates the telescope at Tenerife. E.P. and B.S. also wish to thank the NOAC for funding during their stay in Beijing. DYY thanks the Observatoire de Paris for his stay, supported by the CAS-CNRS collaboration program.

References

Archontis, V., Moreno-Insertis, F., Galsgaard, K., Hood, A., & O'Shea, E. 2004, A&A, 426, 1047
Archontis, V., Moreno-Insertis, F., Galsgaard, K., & Hood, A. W. 2005, ApJ, 635, 1299
Aulanier, G., Démoulin, P., Schmieder, B., Fang, C., & Tang, Y. H. 1998, Sol. Phys., 183, 369
Berlicki, A., Mein, P., & Schmieder, B. 2006, A&A, 445, 1127
Bernasconi, P. N., Rust, D. M., Georgoulis, M. K., & Labonte, B. J. 2002, Sol. Phys., 209, 119
Bruzek, A. 1967, Sol. Phys., 2, 451
Bungey, T. N., Titov, V. S., & Priest, E. R. 1996, A&A, 308, 233
Chae, J., Wang, H., Lee, C.-Y., Goode, P. R., & Schuehle, U. 1998, ApJ, 497, L109
Chen, P. F., & Priest, E. R. 2006, Sol. Phys., 61
Dara, H. C., Alissandrakis, C. E., Zachariadis, T. G., & Georgakilas, A. A. 1997, A&A, 322, 653
David, K.-H. 1961, Z. Astrophys., 53, 37
Démoulin, P., Bagala, L. G., Mandrini, C. H., Hénoux, J. C., & Rovira, M. G. 1997, A&A, 325, 305
Ellerman, F. 1917, ApJ, 46, 298
Fan, Q.-L., Feng, X.-S., Xiang, C.-Q., & Zhong, D.-K. 2003, Phys. Plasmas, 10, 4575
Fang, C., Tang, Y. H., Xu, Z., Ding, M. D., & Chen, P. F. 2006, ApJ, 643, 1325
Georgoulis, M. K., Rust, D. M., Bernasconi, P. N., & Schmieder, B. 2002, ApJ, 575, 506
Handy, B. N., Acton, L. W., Kankelborg, C. C., et al. 1999, Sol. Phys., 187, 229
Heyvaerts, J., Priest, E. R., & Rust, D. M. 1977, ApJ, 216, 123
Isobe, H., Miyagoshi, T., Shibata, K., & Yokoyama, T. 2005, Nature, 434, 478
Isobe, H., Tripathi, D., & Archontis, V. 2007, ApJ, 657, L53
Karpen, J. T., Antiochos, S. K., & Devore, C. R. 1995, ApJ, 450, 422
Kitai, R. 1983, Sol. Phys., 87, 135
Longcope, D. W. 2005, Liv. Rev. Sol. Phys., 2, 7
López Ariste, A., Aulanier, G., Schmieder, B., & Sainz Dalda, A. 2006, A&A, 456, 725
Magara, T., Antiochos, S. K., Devore, C. R., & Linton, M. G. 2005, in Chromospheric and Coronal Magnetic Fields, ed. D. E. Innes, A. Lagg, & S. A. Solanki, ESA SP-596
Malherbe, J. M., Schmieder, B., Mein, P., et al. 1998, Sol. Phys., 180, 265
Mandrini, C. H., Démoulin, P., Schmieder, B., Deng, Y. Y., & Rudawy, P. 2002, A&A, 391, 317
Mein, P. 2002, A&A, 381, 271
Nindos, A., & Zirin, H. 1998, Sol. Phys., 182, 381
Ning, Z., Innes, D. E., & Solanki, S. K. 2004, A&A, 419, 1141
Pariat, E., Aulanier, G., Schmieder, B., et al. 2004, ApJ, 614, 1099
Qiu, J., Ding, M. D., Wang, H., Denker, C., & Goode, P. R. 2000, ApJ, 544, L157
Rust, D. M., & Keil, S. L. 1992, Sol. Phys., 140, 55
Sainz Dalda, A., & López Ariste, A. 2007, A&A, submitted
Scherrer, P. H., Bogart, R. S., Bush, R. I., et al. 1995, Sol. Phys., 162, 129
Schmieder, B., Raadu, M. A., & Wiik, J. E. 1991, A&A, 252, 353
Schmieder, B., Malherbe, J. M., Mein, P., et al. 1997, in Magnetic Reconnection in the Solar Atmosphere, ed. R. D. Bentley, & J. T. Mariska, ASP Conf. Ser., 111, 43
Schmieder, B., Rust, D. M., Georgoulis, M. K., Démoulin, P., & Bernasconi, P. N. 2004, ApJ, 601, 530
Severny, A. B. 1958, in Electromagnetic Phenomena in Cosmical Physics, ed. B. Lehnert, IAU Symp., 6, 114
Severny, A. B. 1968, in Mass Motions in Solar Flares and Related Phenomena, ed. Y. Oehman, 71
Titov, V. S., Priest, E. R., & Démoulin, P. 1993, A&A, 276, 564
Zachariadis, T. G., Alissandrakis, C. E., & Banos, G. 1987, Sol. Phys., 108, 227